




Cite this: *J. Mater. Chem. C*, 2020, **8**, 5058

Tunable photoluminescence in Sb³⁺-doped zero-dimensional hybrid metal halides with intrinsic and extrinsic self-trapped excitons†

Jun Zhou,^a Mingze Li,^b Maxim S. Molokeev,^{cde} Jiayue Sun,^a Denghui Xu ^{*a} and Zhiguo Xia ^{*bf}

Dopants in luminescent metal halides provide an alternative way for photoluminescence tuning towards versatile optical applications. Here we report a trivalent antimony (Sb³⁺)-doped single crystalline 0D metal halide with the composition of (C₉NH₂₀)₉[Pb₃Cl₁₁](ZnCl₄)₂:Sb³⁺. This compound possessed the coexistence of two emission centers including intrinsic and extrinsic self-trapped excitons (STEs), which are ascribed to [Pb₃Cl₁₁]⁵⁻ clusters and triplet STEs formed by the ³P₁-¹S₀ transition of Sb³⁺. By regulating the Sb³⁺ concentration, the emission can be tuned from green to yellow and finally to orange, which would help to develop optically pumped white light-emitting diodes (WLEDs) with different photometric characteristics. Moreover, this dopant-induced extrinsic STE approach presents a new direction towards tuning the luminescence properties of 0D metal halides, and may find application in environmentally-friendly, high-performance metal halide light emitters.

Received 21st January 2020,
Accepted 3rd March 2020

DOI: 10.1039/d0tc00391c

rsc.li/materials-c

1 Introduction

Organic–inorganic hybrid metal halides have attracted substantial attention for their promising application in solar cells, photo-detectors, low-threshold lasers, and light emitting diodes owing to their long carrier diffusion length, adjustable band gap, and high absorption coefficients.^{1–4} By selecting appropriate organic and inorganic components, three- (3D), two- (2D), one- (1D), and zero dimensional (0D) structures at the molecular level can be achieved.^{5–7} Among these, 0D organic metal halides with broad-band emission and high exciton binding energies have become hot materials due to their unprecedented optoelectronic

properties, in which the metal halide molecular/cluster species are totally isolated from each other by large organic cations.^{8–10}

To date, broad-band emission originating from metal halides is generally considered to derive from efficient self-trapped excitons (STEs). As reported, STEs are transient defects which occur in the excited state of a material with soft lattice and strong electron–phonon coupling and emit photons with a large Stokes shift and broad spectrum.^{11–15} There are normally two types of STEs in metal halides: intrinsic STEs and extrinsic STEs.^{16,17} Most of the STE emission in 0D metal halides reported so far is ascribed to intrinsic STEs, such as the broad-band emission in (C₉NH₂₀)₇(PbCl₄)Pb₃Cl₁₁·CH₃CN, (C₉NH₂₀)₉(ZnCl₄)₂(Pb₃Cl₁₁), and (C₉NH₂₀)₉[Pb₃Br₁₁](MnBr₄)₂, whose luminescence originates from intrinsic STEs formed on anionic polyhedra.^{18–20} Very recently, there have been several reports on extrinsic STEs, which are due to the interaction of strong-phonon coupling or impurity-driven exciton accumulation.^{21–23} Amongst these, Chen discovered Sn-triggered extrinsic STEs in 2D PEA₂PbI₄, which generate broadband extrinsic red to near infrared luminescence with a remarkably enhanced PLQY.²¹ Tang and Xia's group independently reported the luminescence of Cs₂SnCl₆:Sb³⁺, which shows broad-band orange emission from extrinsic triplet self-trapped excitons.^{22,23} The results indicate that it is an efficient method to dope ions into metal halides to form extrinsic STEs to produce interesting luminescence properties. However, there are few studies on reports of the coexistence of intrinsic and extrinsic STEs in some specific 0D metal halides.

^a School of Science, Beijing Technology and Business University, Beijing 100048, P. R. China. E-mail: xudh@btbu.edu.cn

^b The Beijing Municipal Key Laboratory of New Energy Materials and Technologies, School of Materials Sciences and Engineering, University of Science and Technology Beijing, Beijing 100083, China

^c Laboratory of Crystal Physics, Kirensky Institute of Physics, SB RAS, Krasnoyarsk 660036, Russia

^d Siberian Federal University, Krasnoyarsk, 660041, Russia

^e Department of Physics, Far Eastern State Transport University, Khabarovsk, 680021, Russia

^f State Key Laboratory of Luminescent Materials and Devices and Institute of Optical Communication Materials, South China University of Technology, Guangzhou, 510641, China. E-mail: xiazg@scut.edu.cn

† Electronic supplementary information (ESI) available: The crystallographic information file (CIF) of (C₉NH₂₀)₉[Pb₃Cl₁₁](ZnCl₄)₂ is presented. See DOI: 10.1039/d0tc00391c

Trivalent antimony (Sb^{3+}) is an important optically active luminescent ion with red broad-band emission originating from a $^3\text{P}_1-^1\text{S}_0$ transition.^{24–27} Up to now, several articles have reported the luminescence of Sb^{3+} as a matrix or activator in metal halides.^{2,22,23,28} However, to the best of our knowledge, the introduction of Sb^{3+} into metal halides so as to form extrinsic STEs to realize multiple emission can benefit the formation of new emission centres and has not been reported till now. Herein, we select $(\text{C}_9\text{NH}_{20})_9[\text{Pb}_3\text{Cl}_{11}](\text{ZnCl}_4)_2$ as the starting model, by gradually replacing the Zn^{2+} in $[\text{ZnCl}_4]^{2-}$ tetrahedra with Sb^{3+} to form $(\text{C}_9\text{NH}_{20})_9[\text{Pb}_3\text{Cl}_{11}](\text{ZnCl}_4)_2:\text{Sb}^{3+}$. This metal halide exhibits dual-emission, *i.e.*, simultaneous green emission from intrinsic STEs formed on $[\text{Pb}_3\text{Cl}_{11}]^{5-}$ trimer clusters and red emission from extrinsic triplet STEs formed by the $^3\text{P}_1-^1\text{S}_0$ transition of Sb^{3+} as also found in other system.²¹ With increasing Sb^{3+} concentration, the emission can be tuned from green to yellow and finally to orange. The design rule established here will provide an efficient way to obtain multiple emission colors by regulating the ratio of intrinsic and extrinsic STEs in 0D metal halides.

2 Experimental section

2.1 Materials and preparation

All the chemicals were commercially purchased and used without further purification. 1-Butyl-1-methylpyrrolidinium chloride ($\text{C}_9\text{NH}_{20}\text{Cl}$) (99%), lead chloride (PbCl_2) (99.99%), antimony chloride (SbCl_3) (99.99%), zinc chloride (ZnCl_2) (99.99%) and dimethylformamide (DMF) (99.9%) were purchased from Aladdin Co. Ltd (Shanghai, Chin). $(\text{C}_9\text{NH}_{20})_9[\text{Pb}_3\text{Cl}_{11}](\text{ZnCl}_4)_2:\text{Sb}^{3+}$ single crystals were synthesized as follows: $\text{C}_9\text{NH}_{20}\text{Cl}$, PbCl_2 , ZnCl_2 and SbCl_3 were dissolved in DMF under heating and continuous stirring at 323 K. The crystals were obtained by slowly cooling the saturated solution to room temperature with a controlled cooling rate to obtain crystals with different sizes. All chemicals were used as received from the vendors without further purification.

2.2 Characterization methods

The diffraction patterns were collected from single crystals of $(\text{C}_9\text{NH}_{20})_9[\text{Pb}_3\text{Cl}_{11}](\text{ZnCl}_4)_2$ at 298 K using a SMART APEX II X-ray single crystal diffractometer (Bruker AXS, analytical equipment of Krasnoyarsk Center of collective use of SB RAS) equipped with a CCD-detector, graphite monochromator and $\text{Mo K}\alpha$ radiation source. Absorption corrections were applied using the SADABS program. The structures were solved by direct methods using package SHELXS and refined using the SHELXL program.²⁹ All hydrogen atoms were linked with C,N atoms and positioned geometrically as riding on their parent atoms with $U_{\text{iso}}(\text{H}) = U_{\text{eq}}(\text{C,N})$. The DIAMOND program³⁰ is used for the crystal structure plotting. Powder X-ray diffraction (PXRD) data of $(\text{C}_9\text{NH}_{20})_9[\text{Pb}_3\text{Cl}_{11}](\text{ZnCl}_4)_2:\text{Sb}^{3+}$ were obtained using a diffractometer D8 ADVANCE (Bruker) equipped with a VANTEC detector with a Ni filter. The measurements were made using $\text{Cu K}\alpha$ radiation. The structural parameters obtained from single crystal analysis were used as a basis for powder

pattern Rietveld refinement. The refinement was performed using TOPAS 4.2 software.³¹ The morphology and particle size of the powder sample were characterized by scanning electron microscopy (SEM, JEOL JSM-6510). Elemental analysis (C, H and N) of the samples was performed using a vario MACRO cube (Elementar Analysensysteme GmbH, Germany). The room temperature excitation (PLE) and room temperature emission spectra (PL) and the room-temperature decay curves were obtained using an FLSP9200 fluorescence spectrophotometer (Edinburgh Instruments Ltd, U.K.). The luminescence decay curves were obtained using an FLS920 using an nF900 flash lamp as the excitation source. The power-dependent photoluminescence spectra were measured using a 375 nm (LE-LS-375-140TFCA, 1–140 mW) laser.

3 Results and discussion

The crystal structure of $(\text{C}_9\text{NH}_{20})_9[\text{Pb}_3\text{Cl}_{11}](\text{ZnCl}_4)_2$ is determined by using single-crystal X-ray diffraction (SCXRD), and the unit cell corresponds to trigonal symmetry with space group $P31c$. Detailed crystal data and structure refinement parameters are shown in Table S1 (ESI[†]), and one can also find the crystallographic information files (CIFs) of the studied compounds $(\text{C}_9\text{NH}_{20})_9[\text{Pb}_3\text{Cl}_{11}](\text{ZnCl}_4)_2$ in the ESI[†]. Fig. 1a shows the structural model and doping mechanism of as-prepared $(\text{C}_9\text{NH}_{20})_9[\text{Pb}_3\text{Cl}_{11}](\text{ZnCl}_4)_2:\text{Sb}^{3+}$, in which the host $(\text{C}_9\text{NH}_{20})_9[\text{Pb}_3\text{Cl}_{11}](\text{ZnCl}_4)_2$ demonstrates a typical 0D structure with individual $[\text{ZnCl}_4]^{2-}$ tetrahedra and $[\text{Pb}_3\text{Cl}_{11}]^{5-}$ trimer clusters surrounded by large organic cations $\text{C}_9\text{NH}_{20}^+$ (1-butyl-1-methylpyrrolidinium⁺), suggesting a 0D type metal halide structure. As mentioned

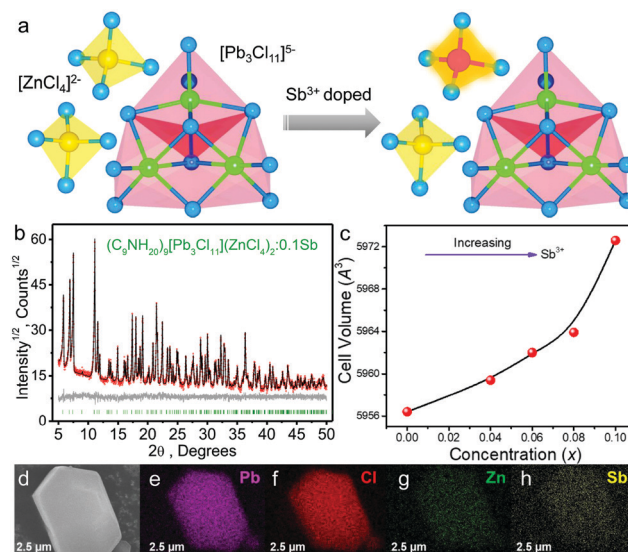


Fig. 1 Diagram of the structural model and doping mechanism of $(\text{C}_9\text{NH}_{20})_9[\text{Pb}_3\text{Cl}_{11}](\text{ZnCl}_4)_2:\text{Sb}^{3+}$. (a) Schematic illustration of the synthesis process of Sb^{3+} doped $(\text{C}_9\text{NH}_{20})_9[\text{Pb}_3\text{Cl}_{11}](\text{ZnCl}_4)_2$ crystals. (b) PXRD profile for Rietveld refinement of $(\text{C}_9\text{NH}_{20})_9[\text{Pb}_3\text{Cl}_{11}](\text{ZnCl}_4)_2:0.1\text{Sb}^{3+}$. (c) Dependence of the unit cell volume from powder pattern Rietveld refinement on different Sb^{3+} doping concentrations. (d–h) SEM and elemental mapping images of Pb, Cl, Zn and Sb for the selected $(\text{C}_9\text{NH}_{20})_9[\text{Pb}_3\text{Cl}_{11}](\text{ZnCl}_4)_2$ particle.

previously, Sb^{3+} -doped metal halides possess interesting optical properties and were widely studied in many systems, which can bestow an intense dopant-sensitized red emission arising from the Sb^{3+} . However, to the best of our knowledge, the introduction of Sb^{3+} into metal halides so as to form extrinsic STEs to realize multiple emission has not been reported. Based on this, we tried to synthesize $(\text{C}_9\text{NH}_{20})_9[\text{Pb}_3\text{Cl}_{11}](\text{ZnCl}_4)_2:\text{Sb}^{3+}$ with the coexistence of intrinsic and extrinsic STEs in order to tune the emission. Fig. S1 (ESI[†]) shows the PXRD patterns of $(\text{C}_9\text{NH}_{20})_9[\text{Pb}_3\text{Cl}_{11}](\text{ZnCl}_4)_2:\text{Sb}^{3+}$ with various Sb^{3+} concentrations. It can be found that all the diffraction peaks can be exactly indexed using the corresponding standard data for the trigonal phase of $(\text{C}_9\text{NH}_{20})_9[\text{Pb}_3\text{Cl}_{11}](\text{ZnCl}_4)_2$, suggesting that doped Sb^{3+} has been successfully dissolved in the $(\text{C}_9\text{NH}_{20})_9[\text{Pb}_3\text{Cl}_{11}](\text{ZnCl}_4)_2$ host lattice. As shown in Fig. 1b, the Rietveld refinement XRD pattern of $(\text{C}_9\text{NH}_{20})_9[\text{Pb}_3\text{Cl}_{11}](\text{ZnCl}_4)_2:0.1\text{Sb}^{3+}$ can prove the successful doping with a pure phase. The unit cell volumes (V) obtained from powder pattern Rietveld refinements of $(\text{C}_9\text{NH}_{20})_9[\text{Pb}_3\text{Cl}_{11}](\text{ZnCl}_4)_2:\text{Sb}^{3+}$ are presented in Fig. 1c. The increase of V illustrates that the lattice positions of Zn^{2+} are gradually substituted by Sb^{3+} ions due to the bigger ionic radius

of Sb^{3+} than that of Zn^{2+} . Fig. 1d shows the SEM images of $(\text{C}_9\text{NH}_{20})_9[\text{Pb}_3\text{Cl}_{11}](\text{ZnCl}_4)_2:\text{Sb}^{3+}$ ($\sim 5 \mu\text{m}$), and the elemental mapping images in Fig. 1e–h indicated that Pb, Cl, Zn and Sb are homogeneously distributed within the particles.

The optical properties of Sb^{3+} -doped $(\text{C}_9\text{NH}_{20})_9[\text{Pb}_3\text{Cl}_{11}](\text{ZnCl}_4)_2$ were fully characterized as discussed below. Fig. 2a shows the images of the pristine and Sb-doped $(\text{C}_9\text{NH}_{20})_9[\text{Pb}_3\text{Cl}_{11}](\text{ZnCl}_4)_2$ under 365 nm excitation at room temperature. $(\text{C}_9\text{NH}_{20})_9[\text{Pb}_3\text{Cl}_{11}](\text{ZnCl}_4)_2$ displays highly bright green emission, and the emission colours of the samples can be tuned from green to yellow and finally to orange with increasing Sb^{3+} concentration. Sb^{3+} has a $5s^2$ outer electronic configuration and the splitting of the energy levels can be expressed as shown in Fig. 2b. The ground state of the Sb ion is $^1\text{S}_0$, whereas the excited state can split into four energy levels: $^3\text{P}_0$, $^3\text{P}_1$, $^3\text{P}_2$ and $^1\text{P}_1$. Based on the transition rules, the transitions of $^1\text{S}_0\text{-}^3\text{P}_2$ and $^1\text{S}_0\text{-}^3\text{P}_0$ are completely forbidden at the electric dipole transition level, but can be induced by lattice vibration, while the transition of $^1\text{S}_0\text{-}^1\text{P}_1$ is allowed and the $^1\text{S}_0\text{-}^3\text{P}_1$ transition is partially allowed owing to spin-orbit coupling for heavy atoms. The photoluminescence within the visible light region is possibly caused by the $^3\text{P}_1\text{-}^1\text{S}_0$ transition.²³ The photoluminescence spectra of $(\text{C}_9\text{NH}_{20})_9[\text{Pb}_3\text{Cl}_{11}](\text{ZnCl}_4)_2:\text{Sb}^{3+}$ at

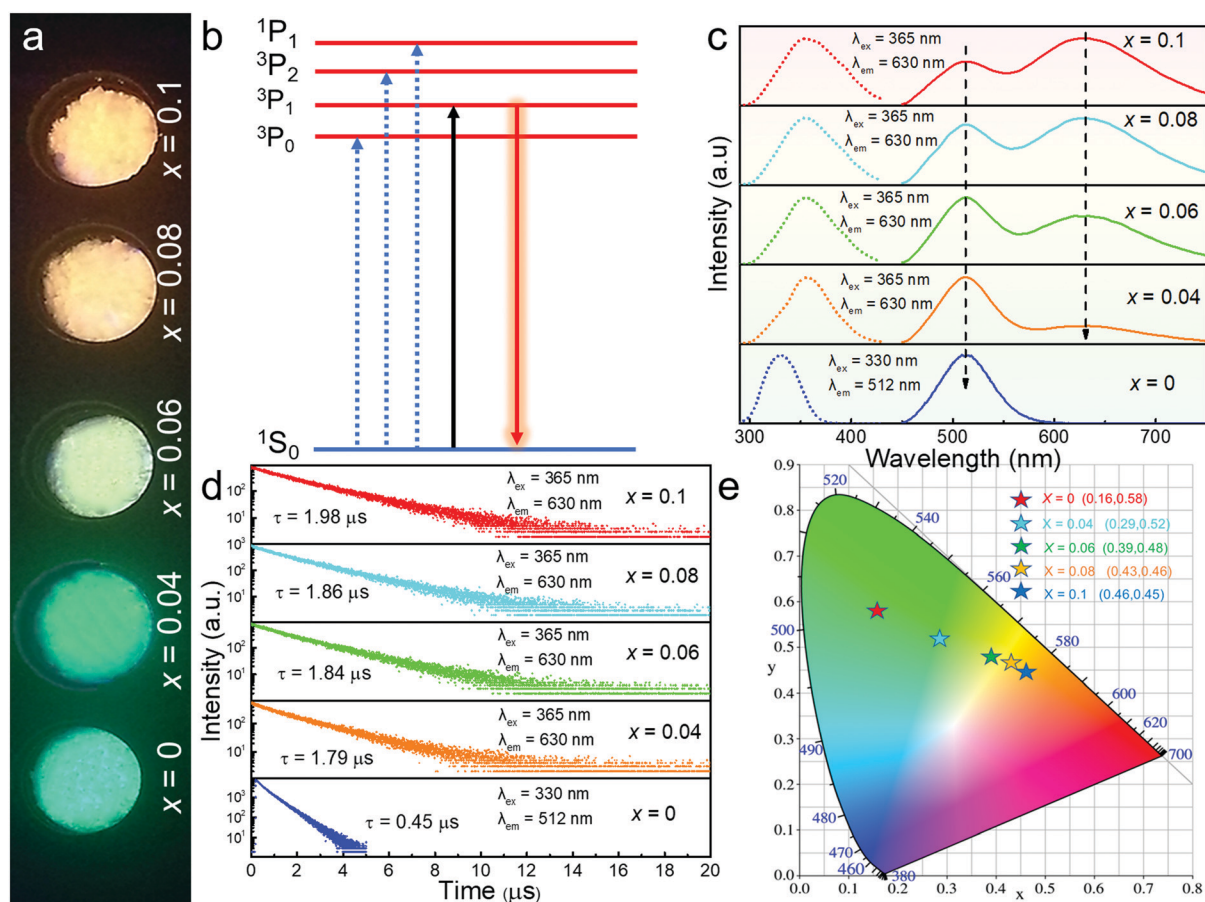


Fig. 2 (a) Digital images of some selected $(\text{C}_9\text{NH}_{20})_9[\text{Pb}_3\text{Cl}_{11}](\text{ZnCl}_4)_2:\text{Sb}^{3+}$ samples under 365 nm UV light. (b) Schematic diagram of the luminescence process for Sb^{3+} in $(\text{C}_9\text{NH}_{20})_9[\text{Pb}_3\text{Cl}_{11}](\text{ZnCl}_4)_2:\text{Sb}^{3+}$. (c) Room-temperature PL and PLE spectra of $(\text{C}_9\text{NH}_{20})_9[\text{Pb}_3\text{Cl}_{11}](\text{ZnCl}_4)_2:\text{Sb}^{3+}$ under different Sb^{3+} concentrations excited at 365 nm and 330 nm. (d) Room-temperature photoluminescence decay curves of $(\text{C}_9\text{NH}_{20})_9[\text{Pb}_3\text{Cl}_{11}](\text{ZnCl}_4)_2:\text{Sb}^{3+}$ depending on the emission wavelengths at 365 nm and 330 nm excitation. (e) CIE chromaticity diagram of $(\text{C}_9\text{NH}_{20})_9[\text{Pb}_3\text{Cl}_{11}](\text{ZnCl}_4)_2:\text{Sb}^{3+}$ excited at 330 nm and 365 nm.

room temperature are shown in Fig. 2c. Upon excitation at 330 nm, $(\text{C}_9\text{NH}_{20})_9[\text{Pb}_3\text{Cl}_{11}](\text{ZnCl}_4)_2$ exhibits bright green emission peaking at 512 nm with a Stokes shift of 182 nm and a full width at half maximum (FWHM) of 61 nm, corresponding to intrinsic STEs of $[\text{Pb}_3\text{Cl}_{11}]^{5-}$ clusters, which is nearly consistent with the reported $(\text{C}_9\text{NH}_{20})_9(\text{ZnCl}_4)_2(\text{Pb}_3\text{Cl}_{11})$.¹⁹ When doping Sb^{3+} ions, besides the green band from $[\text{Pb}_3\text{Cl}_{11}]^{5-}$ clusters, a broad red emission band centered at 630 nm with a large Stokes shift of 265 nm is observed in the PL spectra. The emission at 630 nm is due to the allowed transition ($^3\text{P}_1$ to $^1\text{S}_0$) of Sb^{3+} ions, while the large Stokes shift is due to the fact that the outermost S-P electron orbital transition of Sb^{3+} was highly sensitive to the crystal field distortion of the Sb-Cl polyhedron.^{32,33} With the increase of the Sb^{3+} concentration, $(\text{C}_9\text{NH}_{20})_9[\text{Pb}_3\text{Cl}_{11}](\text{ZnCl}_4)_2:\text{Sb}^{3+}$ exhibited similar PLE spectra, while the ratio of the red emission band intensity to the green emission band intensity increased. Hence, the emission colour of the samples gradually changed from green to yellow and finally to orange, which is consistent with the digital images in Fig. 2a. It is worth noting that there is no energy transfer between $[\text{Pb}_3\text{Cl}_{11}]^{5-}$ clusters and Sb^{3+} here, but a mixture of luminescence from different polyhedrons. The reasons are explained as follows: (1) comparing the PL spectrum of $(\text{C}_9\text{NH}_{20})_9[\text{Pb}_3\text{Cl}_{11}](\text{ZnCl}_4)_2$ and the PLE spectrum of $(\text{C}_9\text{NH}_{20})_9[\text{Pb}_3\text{Cl}_{11}](\text{ZnCl}_4)_2:\text{Sb}^{3+}$, there is little overlap between them; and (2) the PLE spectra of $(\text{C}_9\text{NH}_{20})_9[\text{Pb}_3\text{Cl}_{11}](\text{ZnCl}_4)_2$ and $(\text{C}_9\text{NH}_{20})_9[\text{Pb}_3\text{Cl}_{11}](\text{ZnCl}_4)_2:\text{Sb}^{3+}$ are quite different, suggesting that $(\text{C}_9\text{NH}_{20})_9[\text{Pb}_3\text{Cl}_{11}](\text{ZnCl}_4)_2$ does act as a sensitizer.³⁴ In order to gain insight into the luminescence mechanism of multiple emission centers, the room-temperature decay curves of $(\text{C}_9\text{NH}_{20})_9[\text{Pb}_3\text{Cl}_{11}](\text{ZnCl}_4)_2:\text{Sb}^{3+}$ were measured (Fig. 2d). The emission decay profiles collected at 512 nm of the pristine and 630 nm of the Sb-doped $(\text{C}_9\text{NH}_{20})_9[\text{Pb}_3\text{Cl}_{11}](\text{ZnCl}_4)_2$ are from the contribution of the intrinsic STEs of $[\text{Pb}_3\text{Cl}_{11}]^{5-}$ clusters and extrinsic triplet STEs from the $^3\text{P}_1$ - $^1\text{S}_0$ transition of Sb^{3+} , respectively. All luminescence decay curves can be well fitted with a single order exponential equation:³⁵

$$I(t) = A \exp(-t/\tau) \quad (1)$$

where I is the luminescence intensity, t is the time after excitation, A is a constant and τ is the radiative decay time. Based on eqn (1), the effective decay time of the green band was calculated to be 0.45 μs , while that of the red band with different Sb^{3+} contents was 1.79–1.98 μs . Among them, the long lifetime of microseconds conforms to the characteristics of triplet STEs and is consistent with the previous reports on Sb-doped metal halides.^{2,23,28} Moreover, the lifetime values of Sb^{3+} tend to increase with the increasing content of Sb^{3+} ions, demonstrating that the radiative transition is enhanced in $(\text{C}_9\text{NH}_{20})_9[\text{Pb}_3\text{Cl}_{11}](\text{ZnCl}_4)_2:\text{Sb}^{3+}$. It should be noted that the emission peak of Sb^{3+} here only belongs to the transition of $^3\text{P}_1$ - $^1\text{S}_0$ (triplet), without the transition of $^1\text{P}_1$ - $^1\text{S}_0$ (singlet). Fig. 2e shows the corresponding CIE coordinates of the emission from the pristine and Sb-doped $(\text{C}_9\text{NH}_{20})_9[\text{Pb}_3\text{Cl}_{11}](\text{ZnCl}_4)_2$. By combining the green band from the $[\text{Pb}_3\text{Cl}_{11}]^{5-}$ clusters and red band from the $^3\text{P}_1$ - $^1\text{S}_0$ transition of Sb^{3+} , the emission color tone can be tuned from green (0.16, 0.58) to yellow (0.39, 0.48) and

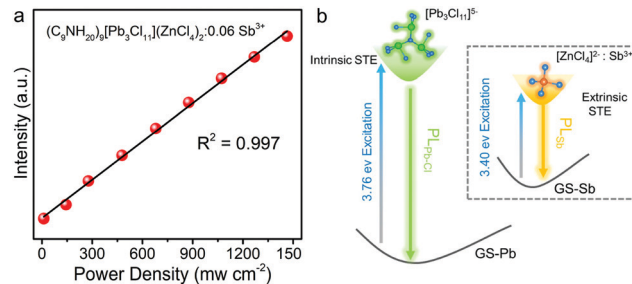


Fig. 3 (a) Dependence of the emission intensity at 630 nm of $(\text{C}_9\text{NH}_{20})_9[\text{Pb}_3\text{Cl}_{11}](\text{ZnCl}_4)_2:0.06\text{Sb}^{3+}$ on the excitation intensity (0–1500 mW cm^{-2}) at 300 K and a linear fit ($\lambda_{\text{ex}} = 375$ nm). (b) Luminescence processes in $(\text{C}_9\text{NH}_{20})_9[\text{Pb}_3\text{Cl}_{11}](\text{ZnCl}_4)_2:\text{Sb}^{3+}$ at room temperature using two configuration diagrams.

finally to orange (0.46, 0.45). The wide colour tunability of $(\text{C}_9\text{NH}_{20})_9[\text{Pb}_3\text{Cl}_{11}](\text{ZnCl}_4)_2:\text{Sb}^{3+}$ would help to develop optically pumped WLEDs with tunable photometric characteristics for different optical applications.

STE emission acts as a typical mechanism that can explain the large Stokes shift of many luminescent metal halide materials.¹⁶ Therefore, we speculate that the luminescence at 630 nm also originates from STEs, just like that at 512 nm. In order to prove it, the variation of the emission intensity excited at 375 nm as a function of the excitation power density was tested and is shown in Fig. 3a. The PL intensity at 630 nm of $(\text{C}_9\text{NH}_{20})_9[\text{Pb}_3\text{Cl}_{11}](\text{ZnCl}_4)_2:0.06\text{Sb}^{3+}$ increases linearly with the excitation power density from 0 to 1500 mW cm^{-2} at 300 K, which further verifies the triplet STEs as the 630 nm emission centers. Therefore, the excited state processes for this 0D organic metal halide hybrid $(\text{C}_9\text{NH}_{20})_9[\text{Pb}_3\text{Cl}_{11}](\text{ZnCl}_4)_2:\text{Sb}^{3+}$ can be depicted as shown in Fig. 3b by using two different configuration diagrams. Upon 330 nm (3.76 eV) excitation, lattice distortion in $[\text{Pb}_3\text{Cl}_{11}]^{5-}$ clusters caused by the strong electron-phonon interactions will prompt the ultrafast formation of STEs, resulting in green emission, while upon 365 nm (3.40 eV) excitation, the $[\text{Pb}_3\text{Cl}_{11}]^{5-}$ clusters are also excited and form STEs, and the rest of the electrons from Sb^{3+} in the ground state are excited, and then undergo ultrafast excited-state reorganization from the high-energy excited states to the triplet STEs following $^3\text{P}_1$ - $^1\text{S}_0$, and exhibit Stokes-shifted red broadband emission. It is worth mentioning that the STEs of $[\text{Pb}_3\text{Cl}_{11}]^{5-}$ clusters are the intrinsic emission centers, while the triplet STEs from the $^3\text{P}_1$ - $^1\text{S}_0$ transition of Sb^{3+} correspond to extrinsic ones by doping.

As a typical example, the green/red dual-emitting $(\text{C}_9\text{NH}_{20})_9[\text{Pb}_3\text{Cl}_{11}](\text{ZnCl}_4)_2:0.06\text{Sb}^{3+}$ has been used in optically pumped LEDs. We fabricated WLEDs by combining our $(\text{C}_9\text{NH}_{20})_9[\text{Pb}_3\text{Cl}_{11}](\text{ZnCl}_4)_2:0.06\text{Sb}^{3+}$ sample, the commercial blue phosphor $\text{BaMgAl}_{10}\text{O}_{17}:\text{Eu}^{2+}$ (BAM:Eu²⁺) and NUV LED InGAN chips ($\lambda = 395$ nm). Fig. 4a shows the PL spectra of the WLED device under a current of 20 mA, and the inset shows the photographs of the fabricated WLED device. The obtained result reveals that the CIE color coordinates are (0.345, 0.360) with a color rendering index (CRI, R_a) of 71.3 and a white light correlated color temperature (CCT) of 4881 K (Fig. 4b). The above results

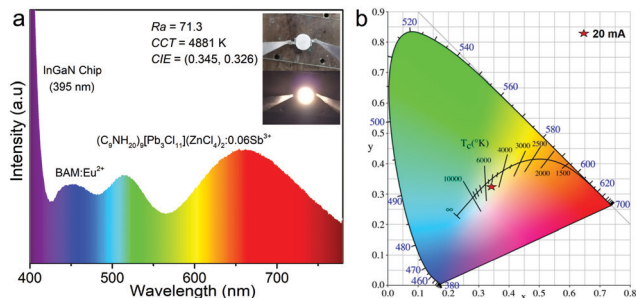


Fig. 4 (a) PL spectra of the WLED fabricated from our phosphor $(\text{C}_9\text{NH}_{20})_9\text{[Pb}_3\text{Cl}_{11}\text{](ZnCl}_4)_2:0.06\text{Sb}^{3+}$ and commercial blue phosphor BAM:Eu $^{2+}$ on a 395 nm InGAN chip at a 20 mA driving current. (b) CIE chromaticity diagram of $(\text{C}_9\text{NH}_{20})_9\text{[Pb}_3\text{Cl}_{11}\text{](ZnCl}_4)_2:0.06\text{Sb}^{3+}$ of the fabricated WLED.

indicate that $(\text{C}_9\text{NH}_{20})_9\text{[Pb}_3\text{Cl}_{11}\text{](ZnCl}_4)_2:0.06\text{Sb}^{3+}$ could be considered as an excellent candidate in the field of NUV WLEDs.

4 Conclusion

In summary, the Sb dopant triggers the occurrence of extrinsic STEs in $(\text{C}_9\text{NH}_{20})_9\text{[Pb}_3\text{Cl}_{11}\text{](ZnCl}_4)_2$ in addition to the intrinsic emission centers originating from STEs of $[\text{Pb}_3\text{Cl}_{11}]^{5-}$ clusters, which enrich the design principles of luminescent metal halides to realize tunable emission colors. By adjusting the doping concentration of Sb^{3+} , the ratio of green emission from intrinsic STEs of $[\text{Pb}_3\text{Cl}_{11}]^{5-}$ clusters and red emission from extrinsic triplet STEs from the $^3\text{P}_1-^1\text{S}_0$ transition of Sb^{3+} is also adjusted, so that the luminescence color of the halide changes remarkably from green to yellow and finally to orange. Such success in 0D metal halides would provide a new perspective for designing superior organic metal halides with multiple emission, which would also allow for the development of optically pumped WLEDs with different photometric properties for various applications.

Conflicts of interest

There are no conflicts to declare.

Acknowledgements

This work is supported by the National Natural Science Foundation of China (No. 51722202, 51961145101, 51972118, 21576002 and 61705003), Fundamental Research Funds for the Central Universities (D2190980), the Guangdong Provincial Science & Technology Project (2018A050506004), and Beijing Technology and Business University Research Team Construction Project (No. PXM2019_014213_000007). This work was also funded by RFBR according to the Research Project No. 19-52-80003.

Notes and references

- P. J. Guo, C. C. Stoumpos, L. L. Mao, S. Sadasivam, J. B. Ketterson, P. Darancet, M. G. Kanatzidis and R. D. Schaller, *Nat. Commun.*, 2018, **9**, 2019.

- Z. Y. Li, Y. Li, P. Liang, T. L. Zhou, L. Wang and R. J. Xie, *Chem. Mater.*, 2019, **31**, 9363–9371.
- S. Yakunin, B. M. Benin, Y. Shynkarenko, O. Nazarenko, M. I. Bodnarchuk, D. N. Dirin, C. Hofer, S. Cattaneo and M. V. Kovalenko, *Nat. Mater.*, 2019, **18**, 846–852.
- Z. P. Wang, Z. Z. Zhang, L. Q. Tao, N. N. Shen, B. Hu, L. K. Gong, J. R. Li, X. P. Chen and X. Y. Huang, *Angew. Chem., Int. Ed.*, 2019, **58**, 9974–9978.
- L. L. Mao, Y. L. Wu, C. C. Stoumpos, B. Traore, C. Katan, J. Even, M. R. Wasielewski and M. G. Kanatzidis, *J. Am. Chem. Soc.*, 2017, **139**, 11956–11963.
- H. R. Lin, C. K. Zhou, Y. Tian, T. Siegrist and B. W. Ma, *ACS Energy Lett.*, 2017, **3**, 54–62.
- Y. Q. Liao, H. F. Liu, W. J. Zhou, D. W. Yang, Y. Q. Shang, Z. F. Shi, B. H. Li, X. Y. Jiang, L. J. Zhang, L. N. Quan, R. Quintero-Bermudez, B. R. Sutherland, Q. X. Mi, E. H. Sargent and Z. J. Ning, *J. Am. Chem. Soc.*, 2017, **139**, 6693–6699.
- G. Giorgi and K. Yamashita, *J. Phys. Chem. Lett.*, 2016, **7**, 888–899.
- S. Brochard-Garnier, M. Paris, R. Génois, Q. Han, Y. Liu, F. Massuyeau and R. J. A. F. M. Gautier, *Adv. Funct. Mater.*, 2019, **29**, 1806728.
- V. Morad, Y. Shynkarenko, S. Yakunin, A. Brumberg, R. D. Schaller and M. V. Kovalenko, *J. Am. Chem. Soc.*, 2019, **141**, 9764–9768.
- T. Hu, M. D. Smith, E. R. Dohner, M. J. Sher, X. X. Wu, M. T. Trinh, A. Fisher, J. Corbett, X. Y. Zhu, H. I. Karunadasa and A. M. Lindenberg, *J. Phys. Chem. Lett.*, 2016, **7**, 2258–2263.
- M. D. Smith, A. Jaffe, E. R. Dohner, A. M. Lindenberg and H. I. Karunadasa, *Chem. Sci.*, 2017, **8**, 4497–4504.
- M. D. Smith and H. I. Karunadasa, *Acc. Chem. Res.*, 2018, **51**, 619–627.
- G. J. Zhou, M. Z. Li, J. Zhao, M. S. Molochev and Z. G. Xia, *Adv. Opt. Mater.*, 2019, **7**, 1901335.
- L. Zhou, J. F. Liao, Z. G. Huang, J. H. Wei, X. D. Wang, W. G. Li, H. Y. Chen, D. B. Kuang and C. Y. Su, *Angew. Chem., Int. Ed.*, 2019, **58**, 5277–5281.
- S. R. Li, J. J. Luo, J. Liu and J. Tang, *J. Phys. Chem. Lett.*, 2019, **10**, 1999–2007.
- L. Zhou, J. F. Liao, Z. G. Huang, J. H. Wei, X. D. Wang, H. Y. Chen and D. B. Kuang, *Angew. Chem., Int. Ed.*, 2019, **131**, 15581–15586.
- C. K. Zhou, H. R. Lin, M. Worku, J. Neu, Y. Zhou, Y. Tian, S. Lee, P. Djurovich, T. Siegrist and B. W. Ma, *J. Am. Chem. Soc.*, 2018, **140**, 13181–13184.
- C. K. Zhou, H. R. Lin, J. Neu, Y. Zhou, M. Chaaban, S. Lee, M. Worku, B. H. Chen, R. Clark, W. H. Cheng, J. J. Guan, P. Djurovich, D. Z. Zhang, X. Lü, J. Bullock, C. Pak, M. Shatruk, M. H. Du, T. Siegrist and B. W. Ma, *ACS Energy Lett.*, 2019, **4**, 1579–1583.
- M. Z. Li, J. Zhou, G. J. Zhou, M. S. Molochev, J. Zhao, V. Morad, M. V. Kovalenko and Z. G. Xia, *Angew. Chem., Int. Ed.*, 2019, **58**, 18670–18675.
- J. C. Yu, J. T. Kong, W. Hao, X. T. Guo, H. J. He, W. R. Leow, Z. Y. Liu, P. Q. Cai, G. D. Qian, S. Z. Li, X. Y. Chen and X. D. Chen, *Adv. Mater.*, 2019, **31**, e1806385.

- 22 J. H. Li, Z. F. Tan, M. C. Hu, C. Chen, J. J. Luo, S. R. Li, L. Gao, Z. W. Xiao, G. D. Niu and J. Tang, *Front. Optoelectron.*, 2019, **12**, 352–364.
- 23 Y. Y. Jing, Y. Liu, J. Zhao and Z. G. Xia, *J. Phys. Chem. Lett.*, 2019, **10**, 7439–7444.
- 24 E. Oomen and G. J. M. R. B. Dirksen, *Mater. Res. Bull.*, 1985, **20**, 453–457.
- 25 E. W. J. L. Oomen, W. M. A. Smit and G. Blasse, *J. Phys. C: Solid State Phys.*, 1986, **19**, 3263.
- 26 L. Chen, A.-Q. Luo, Y. Zhang, X.-H. Chen, H. Liu, Y. Jiang, S.-F. Chen, K.-J. Chen, H.-C. Kuo and Y. Tao, *J. Solid State Chem.*, 2013, **201**, 229–236.
- 27 R. Reisfeld, L. Boehm and B. Barnett, *J. Solid State Chem.*, 1975, **15**, 140–150.
- 28 C. K. Zhou, H. R. Lin, Y. Tian, Z. Yuan, R. Clark, B. Chen, L. J. van de Burgt, J. C. Wang, Y. Zhou, K. Hanson, Q. J. Meisner, J. Neu, T. Besara, T. Siegrist, E. Lambers, P. Djurovich and B. W. Ma, *Chem. Sci.*, 2018, **9**, 586–593.
- 29 G. M. Sheldrick, *Acta Crystallogr., Sect. A: Found. Crystallogr.*, 2008, **64**, 112–122.
- 30 K. Brandenburg and M. Berndt, DIAMOND - Visual Crystal Structure Information System CRYSTAL IMPACT, Postfach 1251, D-53002 Bonn, 2004.
- 31 TOPAS, V.2: General profile and structure analysis software for powder diffraction data—User's Manual; Bruker AXS: Karlsruhe, Germany, 2008.
- 32 R. Reisfeld, L. Boehm and B. Barnett, *J. Solid State Chem.*, 1975, **15**, 140–150.
- 33 E. W. J. L. Oomen, W. M. A. Smit and G. Blasse, *J. Phys. C: Solid State Phys.*, 1986, **19**, 3263.
- 34 S. R. Li, Q. S. Hu, J. J. Luo, T. Jin, J. Liu, J. H. Li, Z. F. Tan, Y. B. Han, Z. Zheng, T. Y. Zhai, H. S. Song, L. Gao, G. D. Niu and J. Tang, *Adv. Opt. Mater.*, 2019, **7**, 1901098.
- 35 Z. F. Tan, J. H. Li, C. Zhang, Z. Li, Q. S. Hu, Z. W. Xiao, T. Kamiya, H. Hosono, G. D. Niu, E. Lifshitz, Y. B. Cheng and J. Tang, *Adv. Funct. Mater.*, 2018, **28**, 1801131.